Corrosion Science 179 (2021) 109153

Contents lists available at ScienceDirect

Corrosion Science

journal homepage: www.elsevier.com/locate/corsci

Determination of thickness and air-void distribution within the iron carbonate layers using X-ray computed tomography

Cailin Wang [a,b], Yong Hua [b,*], Sadegh Nadimi [b,c,*], Wassim Taleb [b], Richard Barker [b], Yuxing Li [a], Xiaohui Chen [d], Anne Neville [b]

[a] Shandong Provincial Key Laboratory of Oil & Gas Storage and Transportation Security, China University of Petroleum (East China), Qingdao, 266555, China
[b] Institute of Functional Surfaces, School of Mechanical Engineering, University of Leeds, Leeds, LS2 9JT, United Kingdom
[c] School of Engineering, Newcastle University, Newcastle upon Tyne, NE1 7RU, United Kingdom
[d] School of Civil Engineering, University of Leeds, Leeds, LS2 9JT, United Kingdom

ARTICLE INFO

Keywords:
CO_2 corrosion
$FeCO_3$
μCT
Porosity

ABSTRACT

Iron carbonate ($FeCO_3$) is a common corrosion product reported in oil and gas fields. The growth kinetics and the presence of connected voids within this layer have a significant influence on the protective capability afforded to the steel surface. X-ray micro-computed tomography (μCT) was used in conjunction with novel algorithms to determine the thickness and air-void distribution within the crystalline $FeCO_3$ layer. Then the relationship between the air-void distribution and corrosion behaviour was analysed. Mercury intrusion porosimetry (MIP) was used to validate the μCT results. The advantages and limitations of both methods for the pore characterisation were discussed.

1. Introduction

Internal carbon dioxide (CO_2) corrosion of carbon steel pipeline is an important problem encountered in the oil and gas industry [1–7]. The formation of corrosion products has a significant effect on the corrosion mechanism and corrosion rate of the underlying steel substrate [8,9]. Depending on the exposed environments and operating conditions, notable differences can be found in the composition and properties of corrosion products [10–13]. Typically, iron carbonate ($FeCO_3$) is the common corrosion product observed on the surface of carbon steel immersed in a NaCl solution saturated with CO_2 [14,15]. However, at the higher temperature, changes in thickness and grain sizes of the $FeCO_3$ layer have been found as well as transitions in the surface species formed, with magnetite (Fe_3O_4) being commonly reported [16,17].

Researchers have studied the effects of operating and environmental conditions on $FeCO_3$ precipitation including temperature, CO_2 partial pressure, pH and brine chemistry. Dugstad [18] reported that dense crystalline films were formed which gave good protection at high temperatures of more than 60 °C. Moreover, Yin et al. [19] showed that the thickness of $FeCO_3$ layer decreased while the protectiveness increased with increasing temperature from 50 to 180 °C for carbon steel exposed to CO_2 environments. A recent study by Hua et al. [20] indicated that increasing temperature from 90 to 250 °C whilst maintaining pH at 4.9 resulted in a reduction in $FeCO_3$ crystal coverage on X65 carbon steel at the expense of the formation of Fe_3O_4. As for the effects of CO_2 partial pressure, Videm et al. [21] showed that increasing partial pressure from 1 bar to 10 bar for an 80 °C brine at approximately pH 5 resulted in faster film formation on carbon steel. Furthermore, Hua et al. [20] reported that increasing CO_2 partial pressure from 2.7 bar to 28.5 bar increased the quantity of $FeCO_3$ on the steel surface at 200 °C with the initial pH was maintained at 5.4.

$FeCO_3$ film growth depends primarily on the kinetics of scale formation [22]. As more $FeCO_3$ precipitates, the film typically grows in density as well as thickness [18]. Li et al. [23] and Gao et al. [24] showed that the $FeCO_3$ films on carbon steel were composed of an inner layer and an outer layer. Though $FeCO_3$ was the major component for both layers, the inner layer was relatively thick and dense, and was consequently attributable to the better protective performance. Current practice is to estimate the thickness of the corrosion product layer based on the cross-sectional scanning electron microscopy (SEM) observation [8–24]. However, the SEM image is a 2D method and locally measures the thickness of corrosion products from a material surface and the subjective effects can cause inaccuracy.

Air-voids between the film and the steel surface can be generated

* Corresponding authors at: Institute of Functional Surfaces, School of Mechanical Engineering, University of Leeds, Leeds, LS2 9JT, United Kingdom.
E-mail addresses: Y.Hua@leeds.ac.uk (Y. Hua), Sadegh.Nadimi-Shahraki@newcastle.ac.uk (S. Nadimi).

https://doi.org/10.1016/j.corsci.2020.109153
Received 4 June 2020; Received in revised form 19 November 2020; Accepted 20 November 2020
Available online 24 November 2020

continuously because of the corrosion processes, affecting the protectiveness of the $FeCO_3$ corrosion product [25,26]: (1) The porous $FeCO_3$ film provides local protection for the steel surface, as the substrate is partially covered with the film and there are connected inner channels for ion transportation; (2) The dense and compact crystalline $FeCO_3$ layer, acting as a barrier against the transport of chemical species between the solution and steel surface, can protect the substrate more efficiently.

To characterise the morphology of $FeCO_3$ films, volumetric porosity (ε) was proposed since it is used as a principal film parameter affecting the transport of species [25]. Furthermore, ε is a necessary parameter for some mechanistic models for CO_2 corrosion prediction [26]. Currently, mass loss and gas adsorption methods have been used to determine the porosity of $FeCO_3$ films. Sun et al. [27] used mass loss method combined with SEM images to calculate the porosity at different temperatures and reaction times under the conditions of pH 6.6 and initial Fe^{2+} concentration 50 ppm. The results showed that the average porosity decreased with the increase of the reaction time and was above 50 % in all cases. The correlations between the porosity of $FeCO_3$ film and the corrosion rate were investigated by Gao et al. [24] via nitrogen adsorption method and a linear relationship between porosity and corrosion rate was found.

Mercury intrusion porosimetry (MIP) is the standard method to determine the pore features within the porous material, which is applicable to detect the pore size ranges between several nanometres and hundreds of micrometres [28–30]. Currently, MIP method has not been applied to the porosity or pore size measurements for corrosion products. Both nitrogen adsorption and MIP techniques can determine the overall porosity of an entire $FeCO_3$ layer. However, these techniques are not able to visualise the air-void or reveal the local layer porosity along with the $FeCO_3$ thickness [31,32]. Additionally, only connected pores can be detected by the nitrogen adsorption or the MIP technique because of the nature of their measuring principles [28,29]. Besides the porosity, the tortuosity or connectivity between the pores within the corrosion product film can also have a significant effect on the transport property referring to some porous medium research [33–36], while these parameters have not been investigated by previous corrosion-related studies.

X-ray micro-computed tomography (μCT) is an advanced technique that allows the three-dimensional (3D) investigation of materials and enables the quantification of microstructural features on the micron length scale [37,38]. The main advantage of μCT is that it is non-destructive without interfering with the chemistry and morphology of the material [39]. μCT has already been successfully used to study steel corrosion [39–43], cement and concrete [34–36,44–46], voids and defects in materials [47–49]. For instance, the spatial distribution of voids and the permeability of concrete were examined by some researchers [34]. Morphological features of pores, the porosity and tortuosity-connectivity of cement mortar were also computed and simulated [36].

As for the application of μCT in steel corrosion, Itty et al. [39] investigated the propagation of corrosion of steel embedded in cement paste and established μCT as a powerful tool to analyse the mechanism of steel corrosion. The development of the corrosion products and the crack formation were observed in the case of carbon steel and stainless-steel reinforcement. In addition, pitting corrosion of stainless steel has also been investigated by μCT. Ghahari et al. [40] used μCT to observe the growth of pits at the tip of stainless-steel pins. The study of Almuaili et al. [41] observed the formation of three discrete pits and showed that the pit volumes obtained by μCT correlated well with the rate predicted by Faraday's law. Moreover, Farhad et al. [42] designed a laboratory apparatus to undertake in-situ μCT monitoring of corrosion fatigue in hydrogen sulphide (H_2S) corrosion environments under uniaxial fatigue loading. The results show that the corrosion pit-to-crack transition in X65 steel in H_2S saline solutions can be investigated by in-situ μCT. A recent study by Rizzo et al. [43] used μCT to qualitatively analyse the $FeCO_3$ scale formed on 1Cr steel samples exposed to CO_2 saturated aqueous solutions at 80 °C and 40 °C. This study proves the capability of μCT in corrosion product morphology observation: protective $FeCO_3$ formation with three different layers were observed at 80 °C while the corrosion products formed at 40 °C were loose and porous. Though μCT has been applied in several steel corrosion studies, little quantitative analysis was carried out including 3D structure analysis, the porosity, pore size distribution and pore connectivity within the corrosion products.

In the present study, μCT is used to quantitatively investigate the pore-related characterisation of the corrosion product film on the carbon steel surface under different experimental conditions. Advanced image processing methods are employed such as multilevel Otsu thresholding [50,51], watershed method [52] and Canny edge detection [53] with novel algorithms for thickness and porosity calculation. In addition, pore size distribution and pore connectivity within the $FeCO_3$ layers are determined, and the relationship to the corrosion behaviour is discussed. MIP tests are also performed and compared with the μCT results. Additionally, the advantages and limitations of both μCT and MIP techniques are summarised in this study.

2. Material and sample preparation

The sample for μCT and MIP tests was sectioned into a cylinder of diameter 4 mm and height 8 mm with a 2 mm diameter and 5 mm height tip, as shown in Fig. 1. The mass loss samples were machined into discs of 25 mm diameter and thickness of 5 mm. A cylinder sample together with a disc sample was exposed to 650 mL electrolyte within the autoclave. Prior to the start of each experiment, samples were wet ground up to 600 silicon carbide grit paper, degreased with acetone, rinsed with distilled water and dried with compressed air before immersion into the test brine. Additionally, the disc samples were weighed using an electronic balance within an accuracy of 10^{-5} g (W_0) before being placed inside the autoclave. The chemical composition of the steel is provided in Table 1.

All high temperature and high-pressure corrosion experiments were conducted within a high-pressure autoclave. Fig. 2 shows a schematic representation of the autoclave setup. The brine used in all experiments was de-aerated by continuously purging with CO_2 overnight. Samples were placed on a Polyether Ether Ketone (PEEK) sample holder within the autoclave. Before transferring the solution into the autoclave, all the lines were flushed out using high pressure CO_2. The prepared CO_2-saturated brine was then carefully delivered into the autoclave, followed by pressurising to a specific CO_2 partial pressure at 25 °C before heating to the required temperatures. The various test conditions evaluated in this study are provided in Table 2. The starting solution pH at elevated temperature and CO_2 partial pressure was predicted using MultiScale software [20] and are also provided in Table 2. Cylindrical samples immersed under the four conditions are labelled as samples 1, 2, 3, 4 respectively.

After the experiments, all the samples were removed from the autoclave, dried and weighed (W_1), the corrosion products were removed using Clark's solution according to the ASTM G1-03 standard [54]. The sample mass after removal of the corrosion products was recorded as W_2. The total mass loss (W) was calculated by the following Eq. (1)

$$W = W_0 - W_2 \tag{1}$$

The corrosion rate of the sample was calculated via Eq. (2)

$$C_R = \frac{87600W}{t\rho A} \tag{2}$$

Where C_R is the corrosion rate, mm/year; A is exposed surface area, cm^2; ρ is steel density, g/cm^3; and t is the immersion time, hours. The mass loss test at each condition was repeated at least three times to ensure the reproducibility of the results.

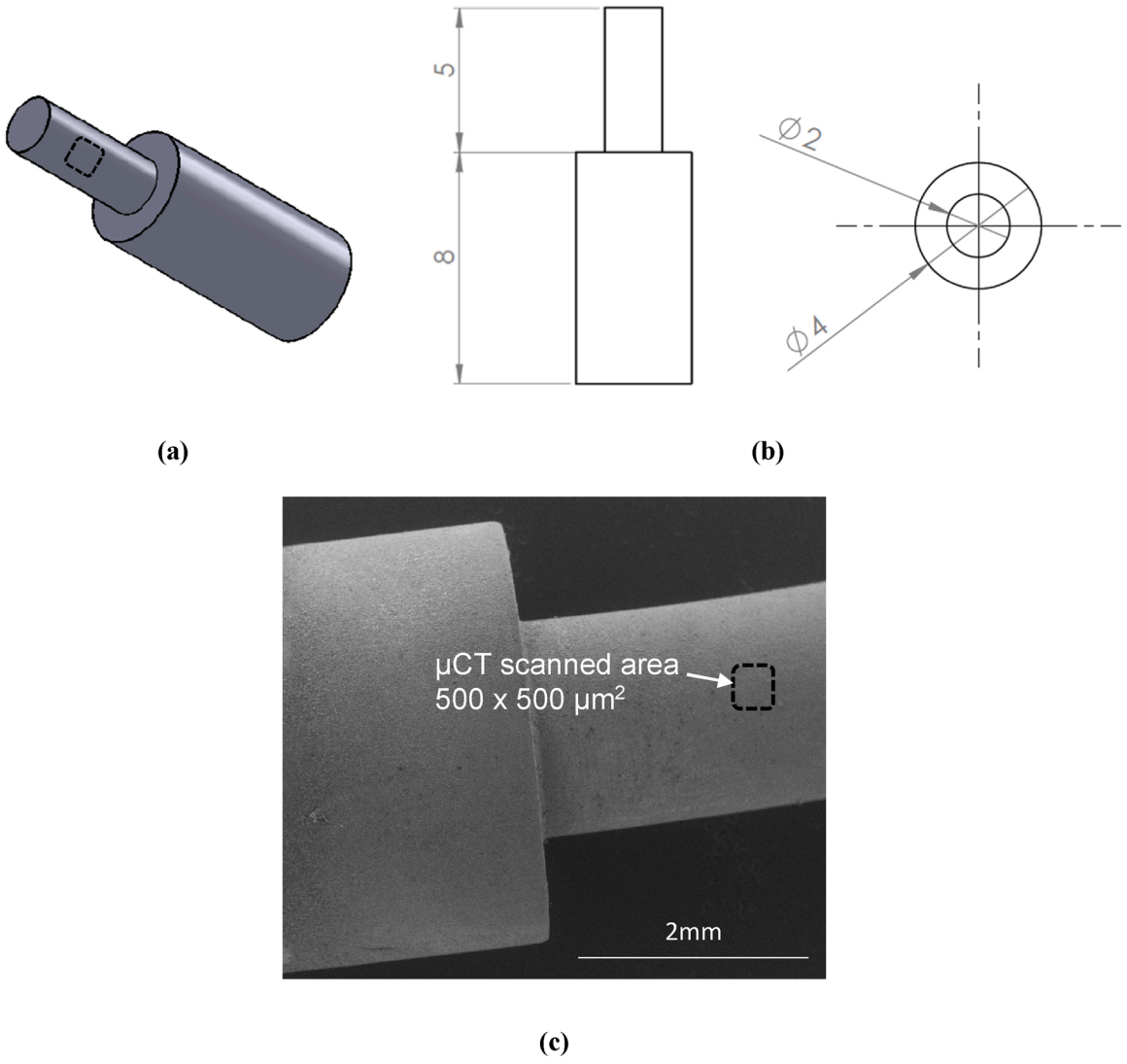

Fig. 1. Cylindrical sample for both μCT and MIP tests **(a)** 3D view; **(b)** section view and top view; **(c)** $FeCO_3$ covered sample.

Table 1
Main elemental compositions of all the materials (wt.%).

C	P	Si	Cr	Mn	Ni	S	Mo
0.12	0.008	0.18	0.11	1.27	0.07	0.002	0.17
Cu	B	Sn	Ti	Al	Fe	Nb	V
0.12	0.0005	0.008	0.001	0.022	Balance	0.054	0.057

3. Microstructure characterisation

3.1. Scanning electron microscopy (SEM)

SEM was used to investigate the surfaces of the corrosion product morphology at high magnification. Information such as size and shape of the surface corrosion products were observed via SEM. SEM images were acquired on a Carl Zeiss EVO MA15 SEM 172 using a 20 keV accelerating voltage.

3.2. X-ray micro-computed tomography (μCT)

μCT was adopted to investigate the spatial distributions of air-voids for the four samples. μCT is a non-invasive and non-destructive method for visualising the inner structures of materials. μCT was performed using an X-Radia 520 VersaScan instrument. The 3D images obtained are maps of x-ray attenuation based on the composition and density of the material. Therefore, each pixel in the image has an intensity value (or colour) associated with the material it represents. A total of 1601 images were captured on a voxel size of $0.538 \times 0.538 \times 0.538\ \mu m^3$ using a 110 kV accelerating voltage and exposure time of 29 s as the sample was rotated through 360°.

3.3. Processing of μCT images

The original x-ray projections received by the CCD detector were converted to digital signals and stored as a data matrix. Based on the data matrix, processing techniques were performed to determine the air-void distribution and porosity within $FeCO_3$ layer.

During the processing procedure as shown in Fig. 3, 8-bit CT images were used for 3D volume reconstruction. Then, a region of interest (ROI) was extracted after which the multilevel Otsu thresholding [50,51] was applied for volume segmentation. After the segmentation, air, corrosion product and steel substrate were labelled with different voxel values as a_{air}, a_{cp} and a_{steel}. Then thickness and porosity calculation within the corrosion product layer were carried out using novel algorithms. In addition, pore size distribution and connectivity of voids were analysed based on the watershed method [52]. All the processing procedures of μCT images were performed on MATLAB R2019a and AVIZO 2019.1.

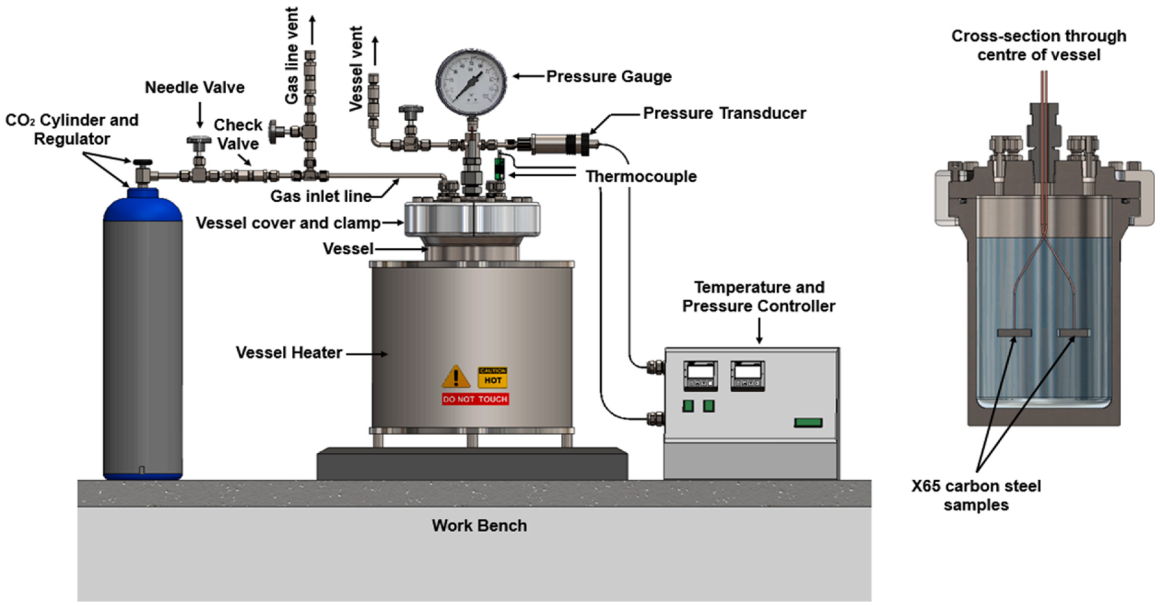

Fig. 2. Schematic of autoclave setup.

Table 2
Test matrix.

Sample No.	Brine composition (mg/L)	Temp (°C)	Measured CO_2 pressure at 25 °C (bar)	Predicted pH at elevated temperature	CO_2 partial pressure (bar)	Total pressure (bar)	Immersion time (hours)
1	NaCl solution, Cl^-: 29503, HCO_3^-: 585	90	10	4.9	13.3	14	48
2	NaCl solution, Cl^-: 29503, HCO_3^-: 25	250	10	4.9	15.4	55	48
3	NaCl solution, Cl^-: 29503, HCO_3^-: 200	200	1	5.4	2.7	18	48
4	NaCl solution, Cl^-: 29503, HCO_3^-: 585	200	20	5.4	28.5	44	48

3.3.1. Image reconstruction

Fig. 4(a) shows a raw 8-bit CT image of sample 1 in which dark grey colour denotes air, light grey colour denotes steel and the middle denotes $FeCO_3$ layer. Based on 500 slices of 2D CT images, a 3D volume can be reconstructed as shown in Fig. 4(b). After reconstruction, a three-dimensional model of the scanned physical zone of the sample was developed, which was composed of 960 × 991 × 500 voxels.

3.3.2. Region of interest (ROI) extraction

To avoid the possible edge effects, a sub-volume was extracted with a cube of 500 × 500 × 500 voxels as the ROI. As an example, the ROI of sample 1 is shown in Fig. 5. Subsequent image processing and analysis were all performed on the ROI.

3.3.3. Image segmentation

As mentioned above, μCT produces images in which the grey value of each voxel is proportional to the density of the corresponding material at that point in space. For an 8-bit grey image, each voxel takes on a value ranging from 0 to 255. In this case, 0 is black corresponding to minimum density, and 255 is white corresponding to maximum density. The densities (20 °C, 1 bar) of air, $FeCO_3$ layer and X65 steel are approximately 1.2, 3900, 7800 kg/m^3 respectively [25,27] so that each phase can be identified based on the significant differences.

To segment the CT images into three distinct phases, it is necessary to firstly select two thresholds in the global histogram [51]. In our study, we calculated the thresholds using Otsu's method that maximises the between-class variance. If the two global thresholds are denoted by I^*_1 and I^*_2 (with $I^*_2 > I^*_1$), then the following criterion on the grey level I of a voxel can be used to identify the three phases:

$$\text{Air-void}: \ I \le I^*_1 \tag{3}$$

$$\text{FeCO}_3\text{layer}: \ I^*_1 \le I \le I^*_2 \tag{4}$$

$$\text{Steelsubstrate}: \ I \ge I^*_2 \tag{5}$$

An example of segmented results is shown in Fig. 6. It can be seen that the air, $FeCO_3$ layer and steel substrate were segmented clearly with different colours, in blue, green and yellow respectively.

By applying the multilevel Otsu thresholding on each slice of the ROI, the 3D volume can then be segmented. It should be noted that each phase has the same voxel value after segmentation and the voxel values for air, $FeCO_3$ layer and steel substrate were a_{air}, a_{cp}, and a_{steel} respectively. The 3D segmented air and $FeCO_3$ layer for sample 1 are displayed separately in Fig. 7.

3.3.4. Quantitative characterisation

Quantitative characterisation of the segmented $FeCO_3$ layer in terms of its thickness distribution, porosity and pore size distribution was carried out. As shown in Figs. 6 and 7, the boundary between steel substrate and corrosion product layer is defined as the inner boundary, while the outer boundary refers to the boundary between air and corrosion product layer. For each thickness calculation, the two boundary points in the same row represented the local thickness, as illustrated in Fig. 8 and the overall thickness distribution was counted row by row in each slice of the ROI.

The porosity ε is defined as

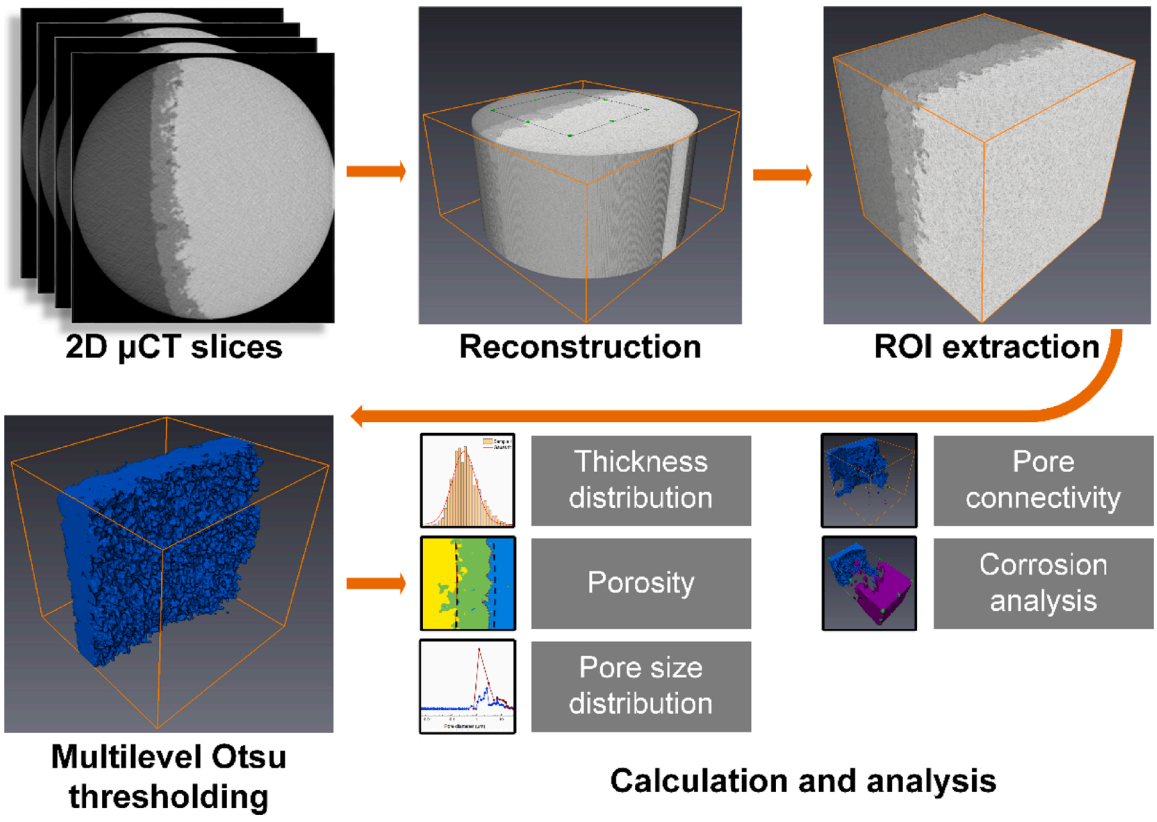

Fig. 3. Steps of μCT image processing and analysis procedure.

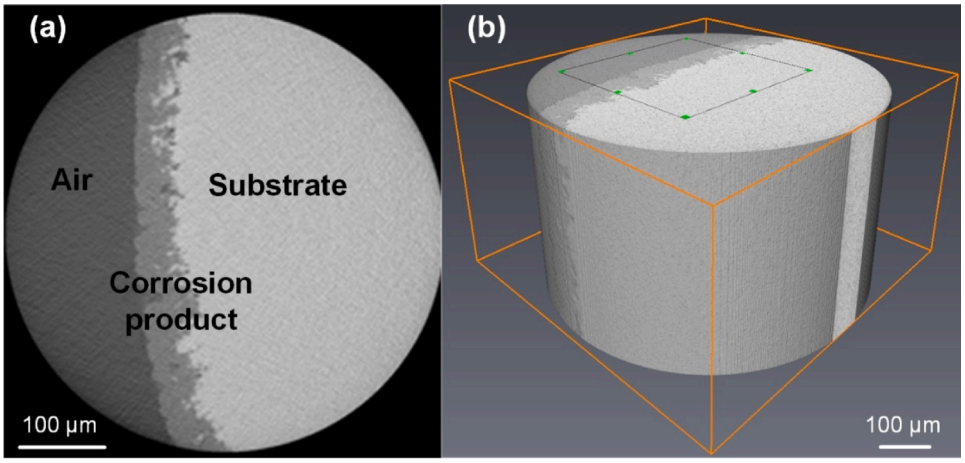

Fig. 4. Reconstruction of μCT images: **(a)** raw 2D image from μCT for sample 1; **(b)** 3D reconstruction.

$$\varepsilon = \frac{V_p}{V_t} = \frac{N_p \times Z_{vox}}{N_t \times Z_{vox}} = \frac{N_p}{N_t} \tag{6}$$

Where ε is the porosity of the sample; V_p is the pore volume of the sample; V_t is the total volume of the sample; N_p is the voxel number of pores; N_t is the voxel number of total volume; Z_{vox} is the spatial voxel size.

As Fig. 9 shows, algorithms were developed in MATLAB for thickness and porosity calculation. Algorithm (a) was used to calculate the thickness distribution, and algorithm (b) was to compute the porosity of the extracted corrosion layer. In both algorithms, Canny edge detection [53] was applied to determine the boundaries of the corrosion products, and the detected boundaries were shown in Fig. 9(a) which fit the actual roughness of the layers well. Then the pores were searched voxel by voxel, and if the voxel value equalled to a_{air}, the voxel was counted as a "void". It should be noted that only the pores (air) distributed within the outer boundary were calculated as shown in Fig. 9(b), which was a limitation for porosity calculation by using Sun's mass loss method [27].

Pore size distribution and pore connectivity analysis were implemented on AVIZO, and the watershed method [37,52] was applied for pore separation considering 26 connectivity (voxels with at least one common vertex were considered as a connected pore).

3.4. Mercury intrusion porosimetry (MIP)

To validate the results of μCT, the MIP method was applied, which is a standard and widely used method to study porous materials [28–30]. MIP is applicable to detect a larger range of pores (from several

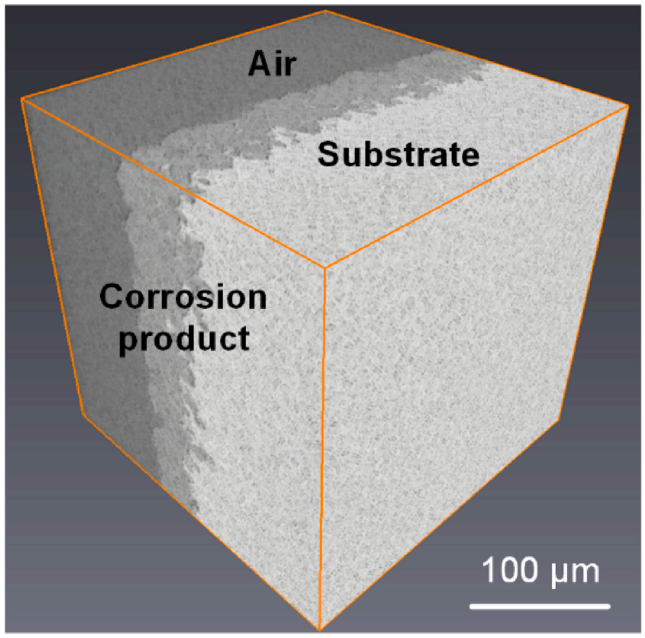

Fig. 5. ROI extraction from sample 1.

nanometres and hundreds of micrometres) compared with μCT. A porosimeter that can detect a minimum pore diameter of 0.002 μm was employed for this study.

The samples were analysed with Micromeritics AutoporeTM IV 9520 system. This model has four low pressure ports and two high pressure chambers. Depending on the penetrometer to be used, 15 samples with the same shape and size for μCT tests were loaded into the penetrometer and evacuated. The penetrometer was automatically backfilled with mercury, and the pressure increments for the volume of mercury introduced were recorded. An automatic blank penetrometer correction and initial data reduction were performed using the Autopore software. The pressure was then plotted against the mercury saturation to produce a capillary pressure curve. The pore size distribution and other properties were calculated from this information.

4. Results and discussion

4.1. Morphology of the corrosion products

SEM images in Fig. 10 show the corrosion products formed on the steel surface after 48 h of exposure at various temperatures and CO_2 partial pressure conditions. The observed corrosion products formed on the surface at 90 °C (Fig. 10(a), sample 1) were visibly dense and compact after 48 h of exposure. As the temperature increased to 250 °C, a less amount of corrosion product was detected and gaps between the crystals appeared on the steel surface (Fig. 10(b), sample 2). It is worth noting that the formation of the corrosion products was less when the samples were exposed to the solution at pH 5.4 and 200 °C with a CO_2 partial pressure of 2.7 bar (Fig. 10(c), sample 3) compared to that at CO_2 partial pressure of 28.5 bar (Fig. 10(d), sample 4). Referring to our previous work [20], the corrosion products were crystalline $FeCO_3$ for sample 1 and 4 (90 °C/13.3 bar CO_2 partial pressure and 200 °C/28.5 bar CO_2 partial pressure respectively). For sample 2 and 3, the corrosion products were mainly comprised of $FeCO_3$ and Fe_3O_4 according to the X-ray diffraction (XRD) and transmission electron microscope (TEM) analysis.

The SEM images suggest that the formation of the corrosion products such as crystalline $FeCO_3$ on the surface is significantly affected by the CO_2 partial pressure or temperature i.e. increased CO_2 partial pressure can favour the crystalline $FeCO_3$ formed on the surface, and the increase in temperature, resulting in the formation of Fe_3O_4 becoming more favourable on the surface [20].

4.2. Thickness and 3D view of the corrosion products

Referring to the literature, the thickness of corrosion products is commonly measured via cross-sectional SEM image and which a 2D method that locally measured the thickness of corrosion products from the material surface. The current corrosion-related studies define the thickness of corrosion products based on the cross-sectional SEM estimation, which is lack of accuracy and reliability as the thickness of corrosion products can be varied from the sample surface. Here a novel evaluation approach for thickness distribution was proposed as shown in the algorithm diagram of Fig. 9. By using this new 3D method, each thickness along the row within the ROI was calculated, thus totally 250,000 thicknesses (500 rows ×500 slices) were counted for each sample. The statistical results for the four samples are shown in Fig. 11. The Gaussian distribution function was used to fit the calculated thickness distributions. The normalised Gaussian distribution function is given by

$$y = y_0 + \frac{A}{w\sqrt{\pi/2}} e^{-2\frac{(x-x_c)^2}{w^2}} \tag{7}$$

$$y = y_0 + \frac{A}{w\sqrt{\pi/2}} e^{-2\frac{(x-x_c)^2}{w^2}}$$

Table 3 presents the Gauss fitting results, showing the x_c and w parameters together with R-squared values. Clearly, the Gaussian distribution function fits well with the thickness distributions. Significant differences in thickness distribution were found for each sample, e.g. the thickness distributed from 20 to 90 μm for sample 1. The results indicate that the mean thickness of the corrosion product layer formed at 90 °C

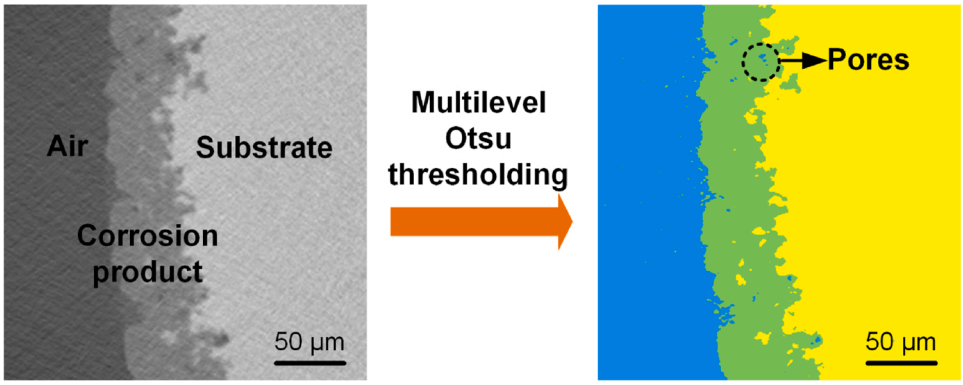

Fig. 6. 2D image segmentation using multilevel Otsu thresholding.

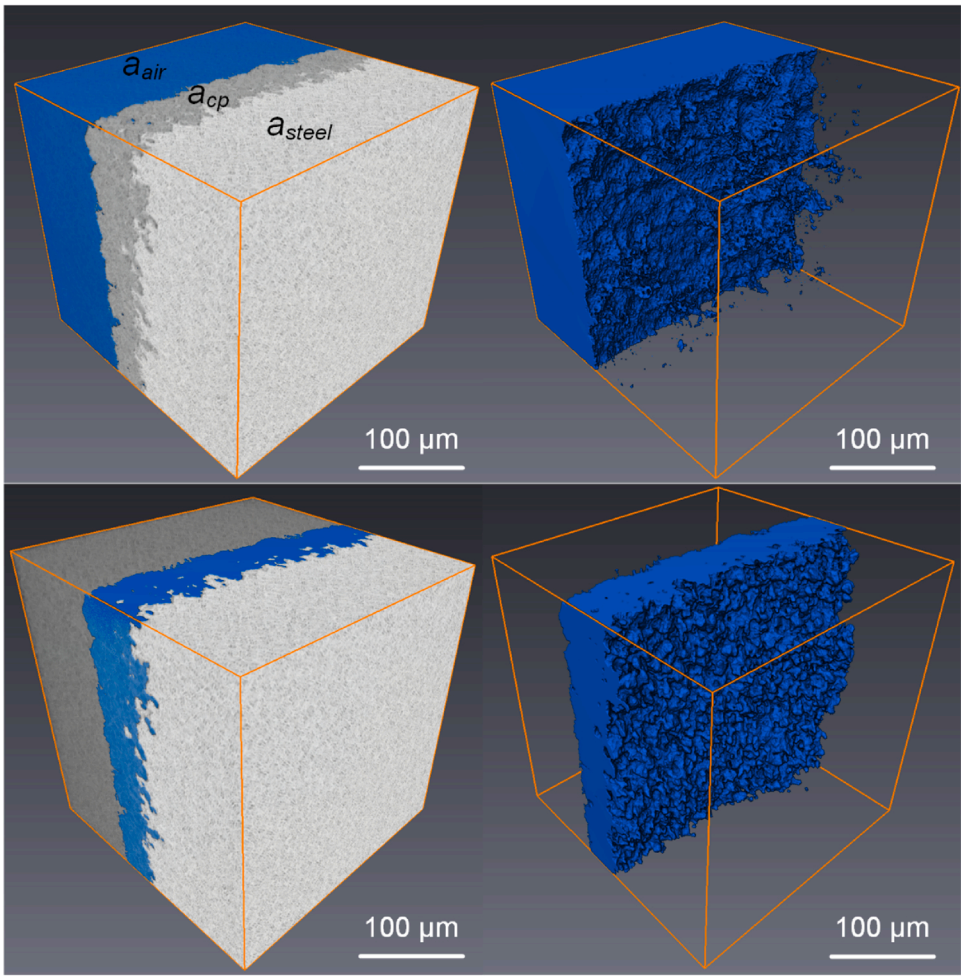

Fig. 7. 3D volume segmentation using multilevel Otsu thresholding. a_{air}, a_{cp}, and a_{steel} are the voxel values of air, corrosion product and steel substrate respectively.

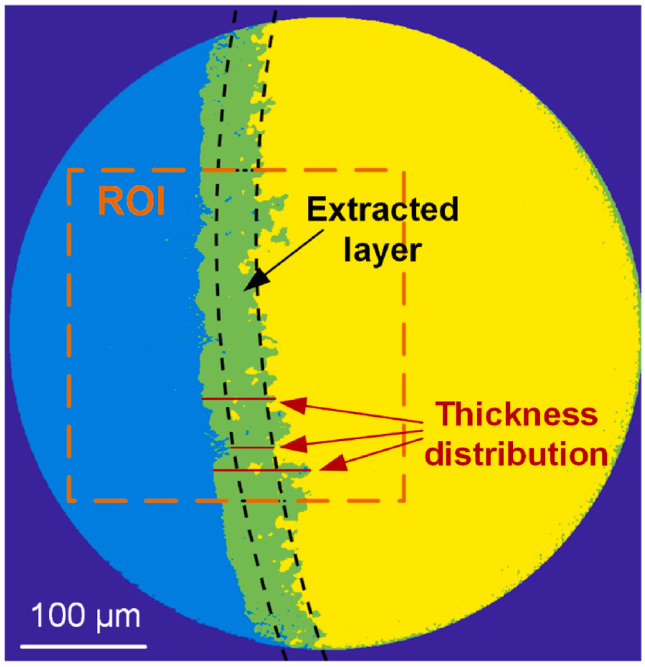

Fig. 8. 2D view of the thickness distribution and annular strip extraction for porosity calculation.

was 50.24 μm. By contrast, increasing temperature from 90 to 250 °C whilst maintaining pH at ~4.9 results in a reduction in the $FeCO_3$ layer thickness to 1.63 μm. At 200 °C and CO_2 partial pressure of 2.7 bar, the thickness was approximately 0.81 μm. When CO_2 partial pressure was increased to 28.5 bar, the $FeCO_3$ layer became thicker and reached 4.53 μm. It is worth noting that nearly 6000 and 16,000 thicknesses were 0 for sample 2 and sample 3 respectively, suggesting that steel surface was not fully covered with corrosion products or the corrosion products were too thin to be detected by μCT, which agrees well with the SEM images in Fig. 10(b) and (c).

The 2D slices and 3D view of corrosion product layers for four samples are shown in Fig. 12, together with the mean thicknesses. Several localised/pitting attack sites were observed on the corroded steel surface (areas A to D) for sample 1 and sample 4. From the 3D views of the corrosion product layers, it can also be found that the inner surface of the corrosion products for sample 1 was the roughest, suggesting the most severe localised corrosion occurred at 90 °C. As the temperature increased from 90 to 250 °C, the interface between corrosion product and corroded steel was noticeably more smooth and showed less localised corrosion, which agreed with our previous observation as Fe_3O_4 is more effective at reducing the susceptibility of the surface to localised corrosion at the conditions evaluated [20]. There were noticeable gaps between the corrosion products for sample 2 and 3, as shown in Fig. 12(d) and (f), which is consistent with the SEM observation in Fig. 10.

The thickness of corrosion products is closely related to the precipitation process. The precipitation/dissolution of $FeCO_3$ is described through the following corrosion reactions [1,55]:

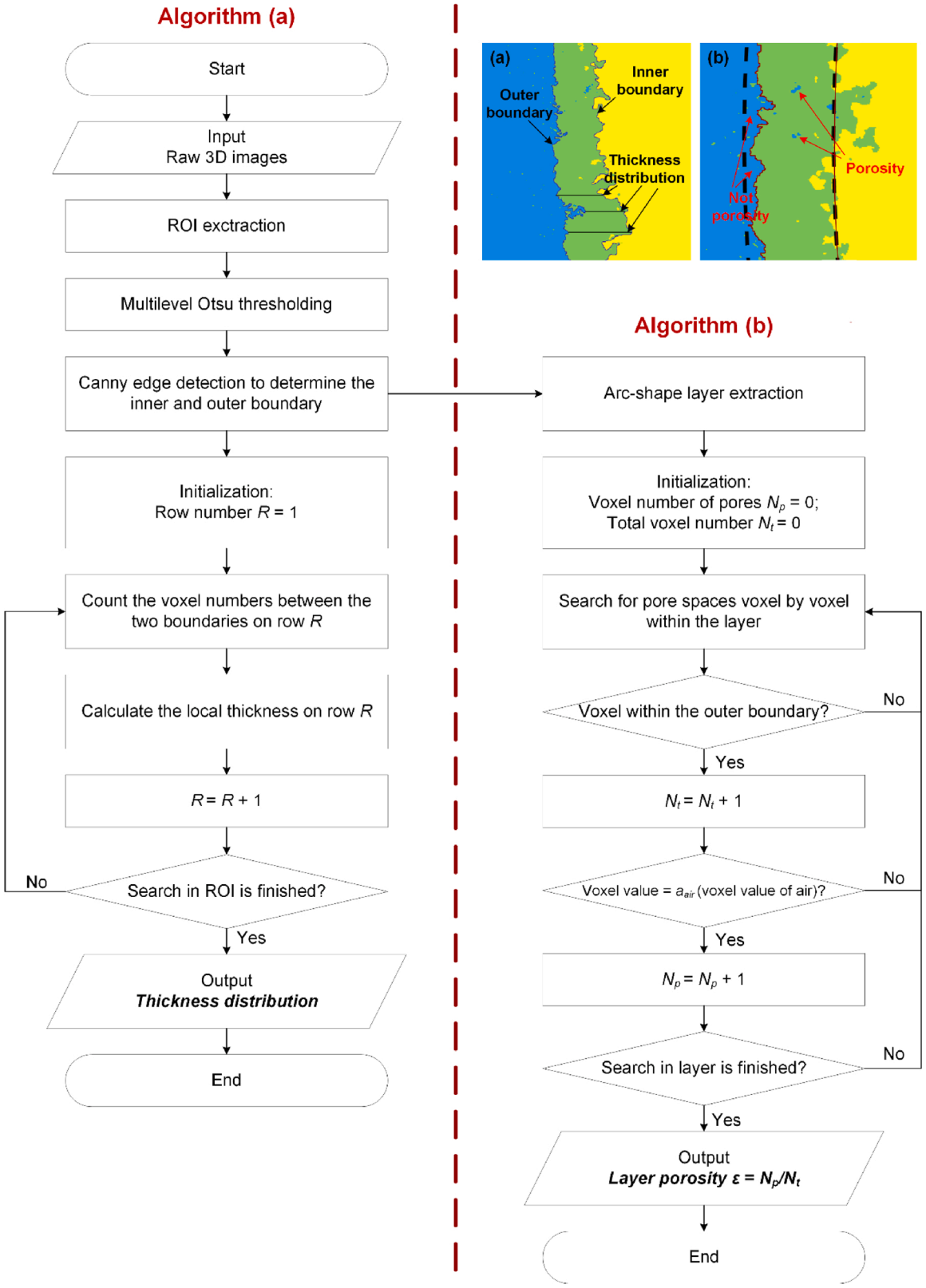

Fig. 9. Algorithms for thickness and porosity calculation. **Algorithm (a)**: To calculate the thickness distribution; **Algorithm (b)**: To calculate the arc-shape layer porosity; **Figure (a)**: Illustration for edge detection and thickness distribution; **Figure (b)**: Illustration for layer porosity calculation, in which the black dashed lines represent the extracted annular strip, the red solid lines represent the actual boundaries in layer porosity calculation (For interpretation of the references to colour in this figure legend, the reader is referred to the web version of this article).

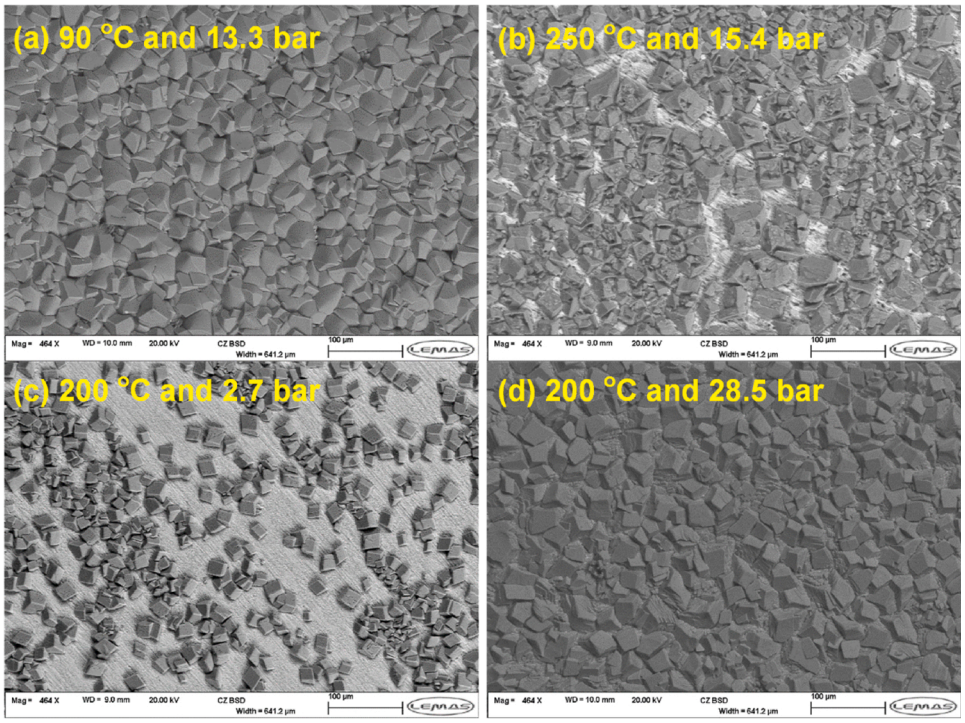

Fig. 10. SEM images of the corrosion products formed on X65 carbon steel surfaces for four samples after 48 h exposure to a CO_2-saturated NaCl brine: **(a) sample 1:** at pH 4.9, 90 °C and CO_2 partial pressure of 13.3 bar; **(b) sample 2:** at pH 4.9, 250 °C and CO_2 partial pressure of 15.4 bar; **(c) sample 3:** at pH 5.4, 200 °C and CO_2 partial pressure of 2.7 bar; **(d) sample 4:** at pH 5.4, 200 °C and CO_2 partial pressure of 28.5 bar.

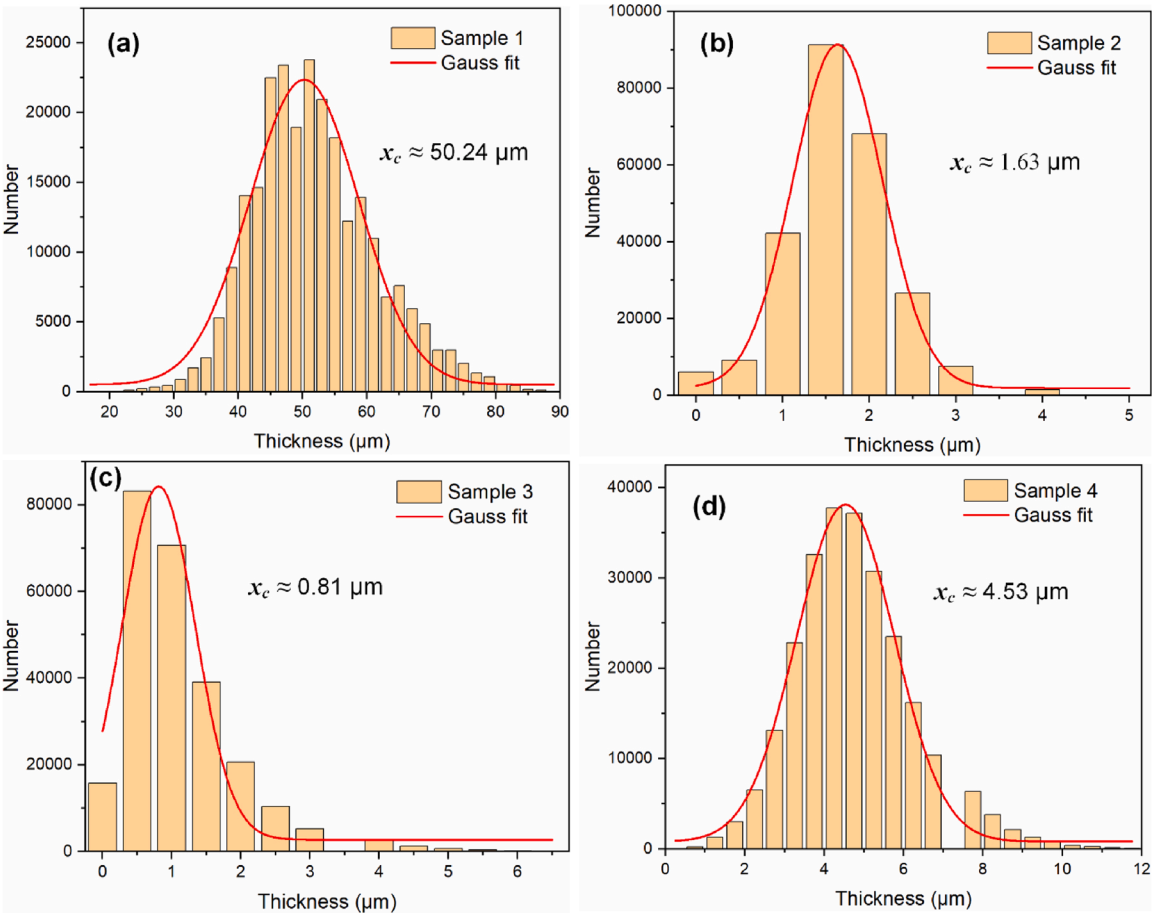

Fig. 11. Thickness distributions and Gauss fits for the corrosion product layers formed on four samples. x_c represents the mean thickness.

Table 3
Thickness calculation using Gaussian distribution function for fitting.

Sample No.	Mean (x_c)	Width (w)	R-squared
1	50.24	16.92	0.96
2	1.63	1.03	0.99
3	0.81	1.06	0.94
4	4.53	2.47	0.98

$$Fe^{2+} + CO_3^{2-} \rightleftharpoons FeCO_3(s) \tag{8}$$

If the product of the concentration of Fe^{2+} and CO_3^{2-} exceeds the saturation limit, the formation of $FeCO_3$ by precipitation is favoured.

$FeCO_3$ supersaturation S is the driving force for precipitation [27]:

$$S = \frac{c_{Fe^{2+}} c_{CO_3^{2-}}}{K_{sp}} \tag{9}$$

Where $c_{Fe^{2+}}$ is the concentration of Fe^{2+}; $c_{CO_3^{2-}}$ is the concentration of CO_3^{2-}; and K_{sp} is the solubility for $FeCO_3$. The relative supersaturation σ is defined as [24]:

$$\sigma = \frac{Q - Q_{eq}}{Q_{eq}} = S - 1 \tag{10}$$

Where Q is the $FeCO_3$ concentration of the solution at any instant, Q_{eq} is the equilibrium solubility of $FeCO_3$.

In terms of the precipitation process of $FeCO_3$ onto a steel surface, the precipitation rate (mol $m^{-2}s^{-1}$) is expressed as [26]:

$$PR = k_r \frac{A}{V} K_{sp}(S-1) = k_r \frac{A}{V}(c_{Fe^{2+}} c_{CO_3^{2-}} - K_{sp}) \tag{11}$$

Where A/V is the ratio of surface area to solution volume, k_r is the kinetic constant, derived from the experimental results as a function of temperature, using Arrhenius's equation [27]:

$$k_r = k_r^0 e^{-\frac{\Delta H}{R}\left(\frac{1}{T}-\frac{1}{T_0}\right)} = e^{A_0 - \frac{B}{RT}} \tag{12}$$

With the following constants: $A_0 = 21.3$ and $B = 64851.4$ J/mol.

Increasing temperature serves to increase the kinetic constant k_r (Eq. 12) and reduce the solubility limit K_{sp} [15,56]. However, the formation of Fe_3O_4 between the steel surface and the $FeCO_3$ layer is thermodynamically more stable at 250 °C, inhibiting the anodic steel dissolution. Thus, the concentration product $c_{Fe^{2+}} c_{CO_3^{2-}}$ drops with increasing temperature, which has a more significant effect on $FeCO_3$ precipitation. As a result, less $FeCO_3$ precipitates on the steel surface at 250 °C according to Eq. (11).

With regard to the effects of CO_2 partial pressure, the increase in CO_2 partial pressure appears to make the formation of $FeCO_3$ more favourable relative to Fe_3O_4 on the surface between 2.7 and 28.5 bar for a constant temperature of 200 °C [20]. Typically, an increase in CO_2 partial pressure will lead to a rise in CO_3^{2-} concentration within the bulk solution, the concentration product $c_{Fe^{2+}} c_{CO_3^{2-}}$ increases with rising CO_2 partial pressure [21]. Thus, an increase in $FeCO_3$ precipitation can be found when CO_2 partial pressure was increased from 2.7 to 28.5 bar based on Eq. (9).

Furthermore, 'blue' regions can be observed within the $FeCO_3$ corrosion products in cross-section μCT images (e.g. Fig. 12(a) and (g)), demonstrating the voids within the corrosion products. 'Yellow' regions can also be seen within the corrosion products on sample 1 which indicates the existence of undissolved carbon steel or Fe_3C. To further investigate the air-void distributions and their effects on corrosion behaviour, the porosity needs to be determined quantitatively.

4.3. Porosity calculations

For the following sections, local porosity of extracted corrosion layer was analysed, followed by various thicknesses and overall porosity of the corrosion products. The calculated results via μCT were discussed and compared with MIP results. Due to the fact that the steel surfaces are not fully covered with $FeCO_3$ and the thickness of corrosion products are too thin which may induce large calculation errors for sample 2 and sample 3, the porosities were only analysed for sample 1 and sample 4.

4.3.1. Local porosity of extracted corrosion layer

Fig. 13 describes the local porosity of extracted $FeCO_3$ layer (the extracted layer has the same width) along with the $FeCO_3$ thickness and it can be noted that the outer layer boundary was determined along with the outer rough $FeCO_3$ surface. The results show that the calculated porosity of both samples increased from the inner to the outer interface, providing direct evidence that the inner layer of $FeCO_3$ was denser than the outer layer. Specifically, the local porosity of extracted layer from sample 1 increased from 0 to around 1.7 % while layer porosity rose from 0 to 3.2 % for sample 4, suggesting that the outer layer was more porous for sample 4. The calculated local porosity for sample 1 and 4 by μCT agrees well with the results of linear polarisation resistance and EIS impedance in Gao's research [24] which showed gaps were generated between the $FeCO_3$ crystals with large grain size, resulting in a relatively high porosity recorded.

4.3.2. Layer porosity along with the thickness of corrosion products

Layer porosity along with the various thickness of the extracted corrosion layer was calculated and the results are shown in Fig. 14. Clearly, rising trends in porosity can be seen for both samples as the thickness of the extracted $FeCO_3$ film increased. The porosity with the largest extraction thickness (overall porosity) for sample 1 rose to 0.57 % at nearly 100 μm, while that for the sample 4 increased to 1.05 % with a thickness of about 13 μm. Thus, the porosity of the whole thickness of corrosion products for sample 4 was larger than that of sample 1.

4.3.3. The relationship between porosity and corrosion behaviour

The general corrosion rates of carbon steels exposed to high temperature and high-pressure CO_2-saturated conditions are shown in Fig. 15. The results indicate that the increase in temperature from 90 to 250 °C whilst maintaining pH at ~4.9 results in a reduction in corrosion rate from 3.2 to 0.9 mm/year. By contrast, the corrosion rate increases slightly from 0.3 to 0.4 mm/year by increasing the CO_2 partial pressure from 2.7 bar to 28.5 bar for the experiments at 200 °C with the pH maintained at 5.4. The corrosion behaviour results suggest that the increase in temperature contributed to a reduction in corrosion rate, however, the increased CO_2 partial pressure has no significant effect on the recorded corrosion rate of carbon steel.

Referring to Fig. 14, the overall porosities for sample 1 and 4 are 0.57 % and 1.05 % respectively, however, the corrosion rate of sample 1 is much larger than sample 4. Obvious gaps between corrosion product crystals are seen on sample 2 and 3 surfaces, suggesting very porous distributions of observable crystalline corrosion products. It is interesting to note that the recorded corrosion rates were relatively lower for sample 2 and 3 though they were not fully covered with corrosion products. In our previous work [20], for sample 2 and 3, it can be found that a Fe_3O_4 layer with a thickness of about 200 nm is formed between the $FeCO_3$ crystal and the steel substrate, which is lower than the resolution of μCT, therefore the Fe_3O_4 layer cannot be detected by μCT measurements. The formation of Fe_3O_4 layer appears to provide better protective performance than the $FeCO_3$ film, reducing the susceptibility of steel surface to general and localised corrosion. Fe_3O_4 is thermodynamically more stable at 250 °C than at 90 °C, and the reduced CO_2 partial pressure from 28.5 bar to 2.7 bar can favour Fe_3O_4 formed on the surface. As a result, lower general corrosion rates were found for sample 2 and 3.

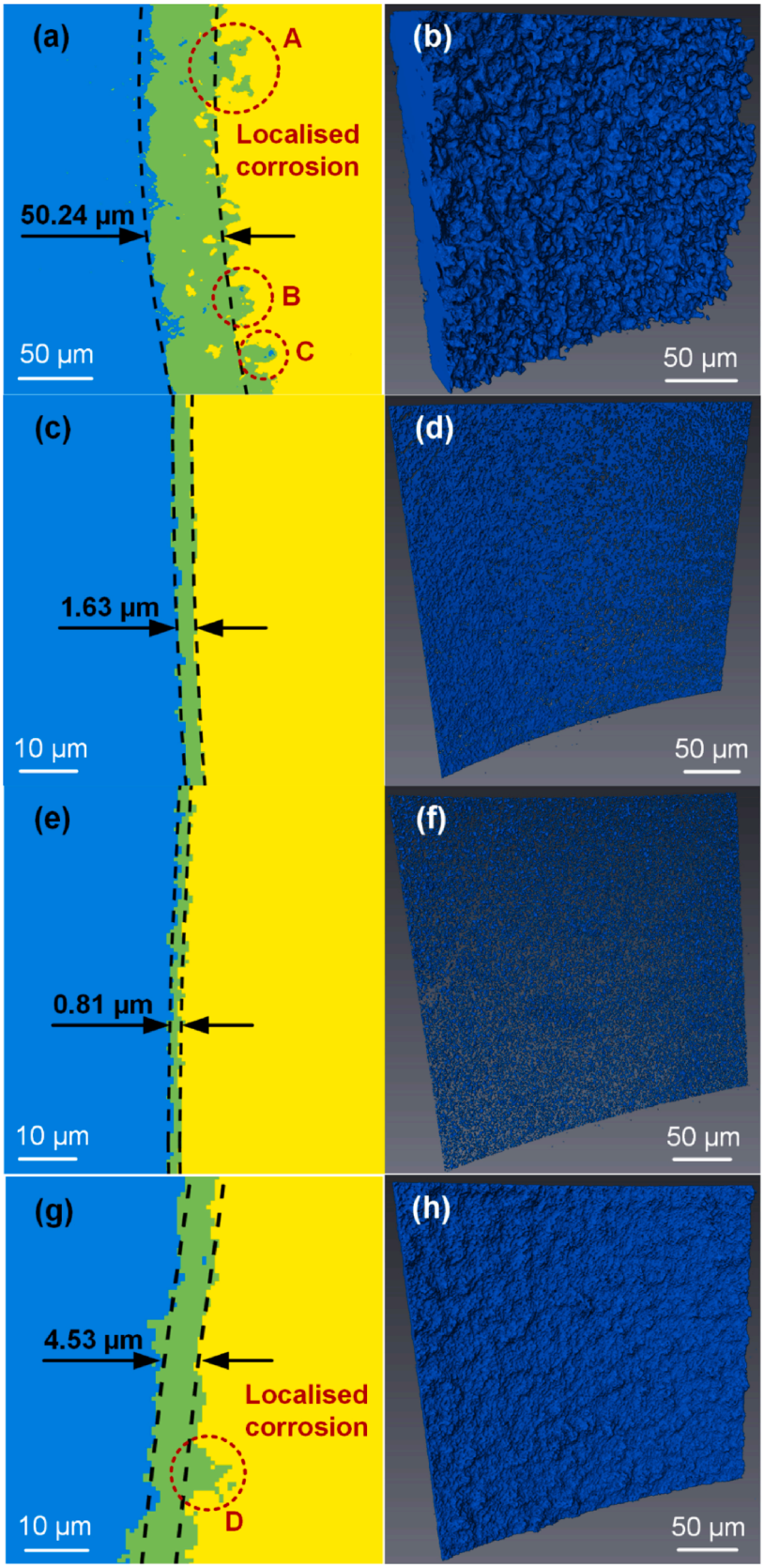

Fig. 12. 2D μCT slices after multilevel Otsu thresholding segmentation and 3D views of the corrosion product layers: **(a, b)** sample 1; **(c, d)** sample 2; **(e, f)** sample 3; **(g, h)** sample 4. The front surfaces in the 3D views are in contact with the corroded steel surfaces.

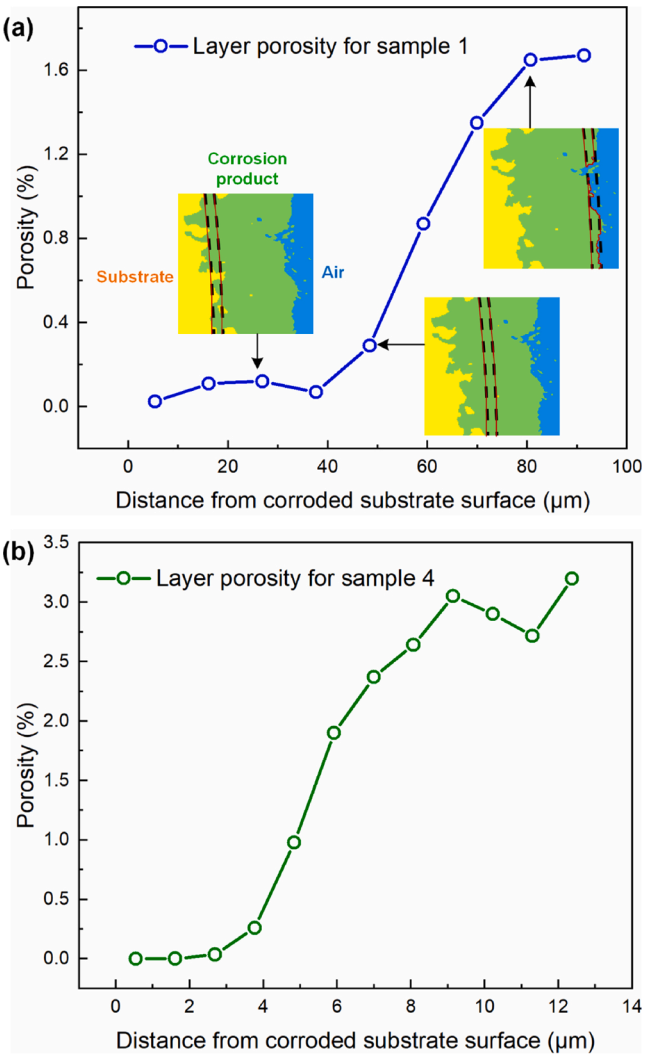

Fig. 13. Local porosity of extracted $FeCO_3$ layer distributed along with $FeCO_3$ thickness from the corroded steel surface: **(a)** sample 1; **(b)** sample 4. The black dashed lines in the illustration represent the boundaries of extracted layer; the red solid lines represent the actual boundaries in the calculation to consider the outer roughness of corrosion product layer (For interpretation of the references to colour in this figure legend, the reader is referred to the web version of this article).

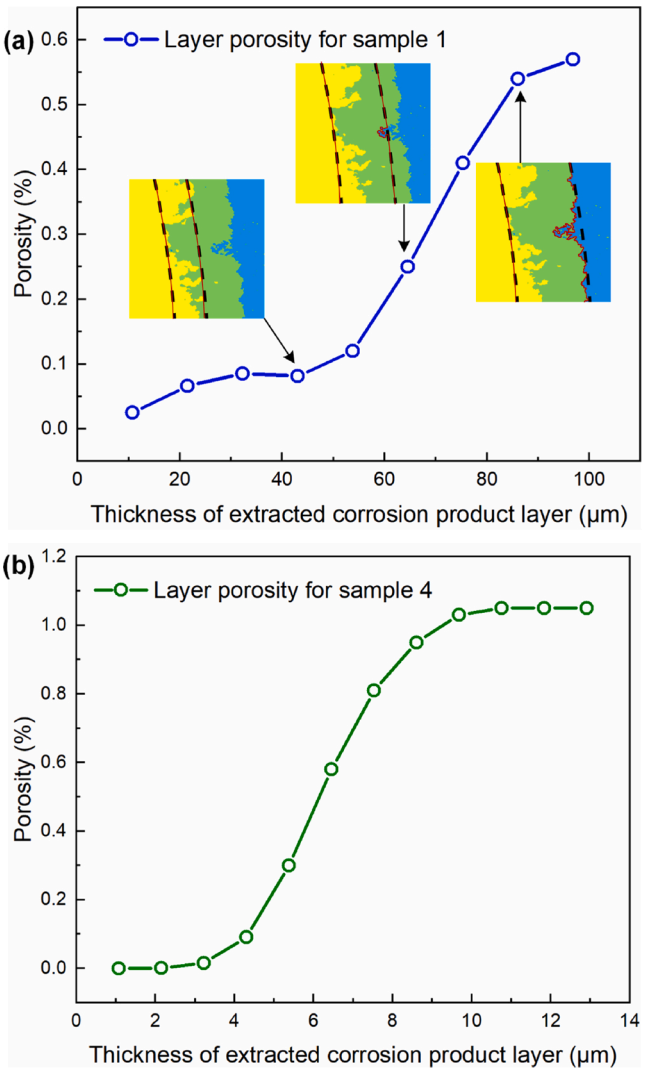

Fig. 14. Porosity of various extracted corrosion layer: **(a)** sample 1; **(b)** sample 4. The black dashed lines in the illustration represent the boundaries of extracted layer; the red solid lines represent the actual boundaries in calculation to consider the effects of outer roughness (For interpretation of the references to colour in this figure legend, the reader is referred to the web version of this article).

Compared with the linear relationship between total porosity and corrosion rate found by Gao et al. [24], our results suggest that the relationship between porosity and corrosion rate is complex and can be highly affected by the experimental conditions (such that the change in porosity with the corrosion product thickness or the presence of the inner Fe_3O_4 layers). Thus there is no direct correlation between porosity and corrosion rate under the current four experimental conditions.

4.4. Pore size distribution

MIP is the standard method to determine the pore feature measurements, which is applicable to detect the pore size ranges between several nanometres and hundreds of micrometres [28–30]. Due to the fact that the pore sizes within the Fe_3O_4 layer cannot be detected by either MIP or μCT measurements accurately, the comparisons were considered to be made only for sample 1 and sample 4.

Based on the assumption of cylindrical pores, the pore size distribution can be calculated by the Washburn Equation [29] for the MIP measurements:

$$d_{MIP} = \frac{-4\gamma\cos\theta}{P} \tag{13}$$

Where P is the absolute injection pressure, MPa; d_{MIP} is the pore diameter (μm) when mercury enters at the pressure P (MPa); θ is the contact angle between mercury and the pore surface (assumed to be 130° in the measurements); and γ is the surface tension of mercury (set to 0.485 N/m^2).

For the μCT calculation of pore size distribution, each pore volume within the $FeCO_3$ layer was examined and separated by the watershed method [37,52]. For a given pore, the equivalent pore diameter equals to the diameter of the spherical volume:

$$d_{CT} = \sqrt[3]{\frac{6V}{\pi}} \tag{14}$$

Where V is the separated pore volume, $\mu m^3$and d_{CT} denotes the equivalent diameter of pores calculated by μCT, μm. This pore statistical approach is different from MIP where the pore information is obtained by the cumulative volume [57]. Though there are some differences in

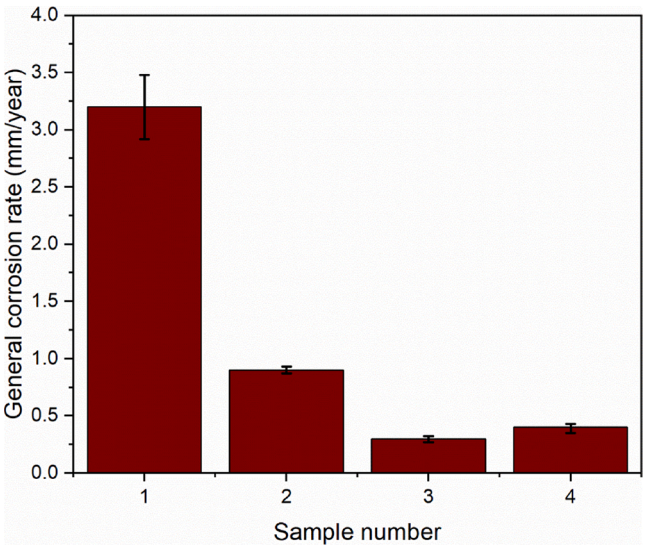

Fig. 15. General corrosion rate for four samples after 48 h immersed in the brine.

the pore size calculation between MIP and μCT, the calculated results by MIP (Eq.13) and μCT (Eq.14) are comparable [33]. The calculated pore size distribution through μCT is shown in Fig. 16 together with the direct measurements via MIP method.

According to the μCT and MIP results (Fig. 16(a)), the pore size distributions indicate that the pore diameter ranges corresponding to the μCT data agree well with MIP results for sample 1, two peaks at diameters of 1.5 μm and 10 μm were observed, and the pore diameters are mainly in the range from 1 μm to 5 μm by both methods. For sample 4, smaller pore sizes at sub-micron level were observed via MIP, while these pores were not able to be detected by μCT due to its spatial resolution limitation. Therefore, the overall porosity value of sample 4 calculated by μCT was notably lower than that of MIP method, as shown in Fig. 16(c).

However, both μCT and MIP results demonstrate that the overall porosity of sample 4 is larger than that of sample 1. The pore sizes became smaller as the temperature and pressure increased from 90 °C and 13.3 bar of CO_2 partial pressure to 200 °C and 28.5 bar of CO_2 partial pressure, suggesting that small pore sizes were related to the fast kinetics as the crystalline $FeCO_3$ formed quicker on the surface under higher temperature and CO_2 partial pressure.

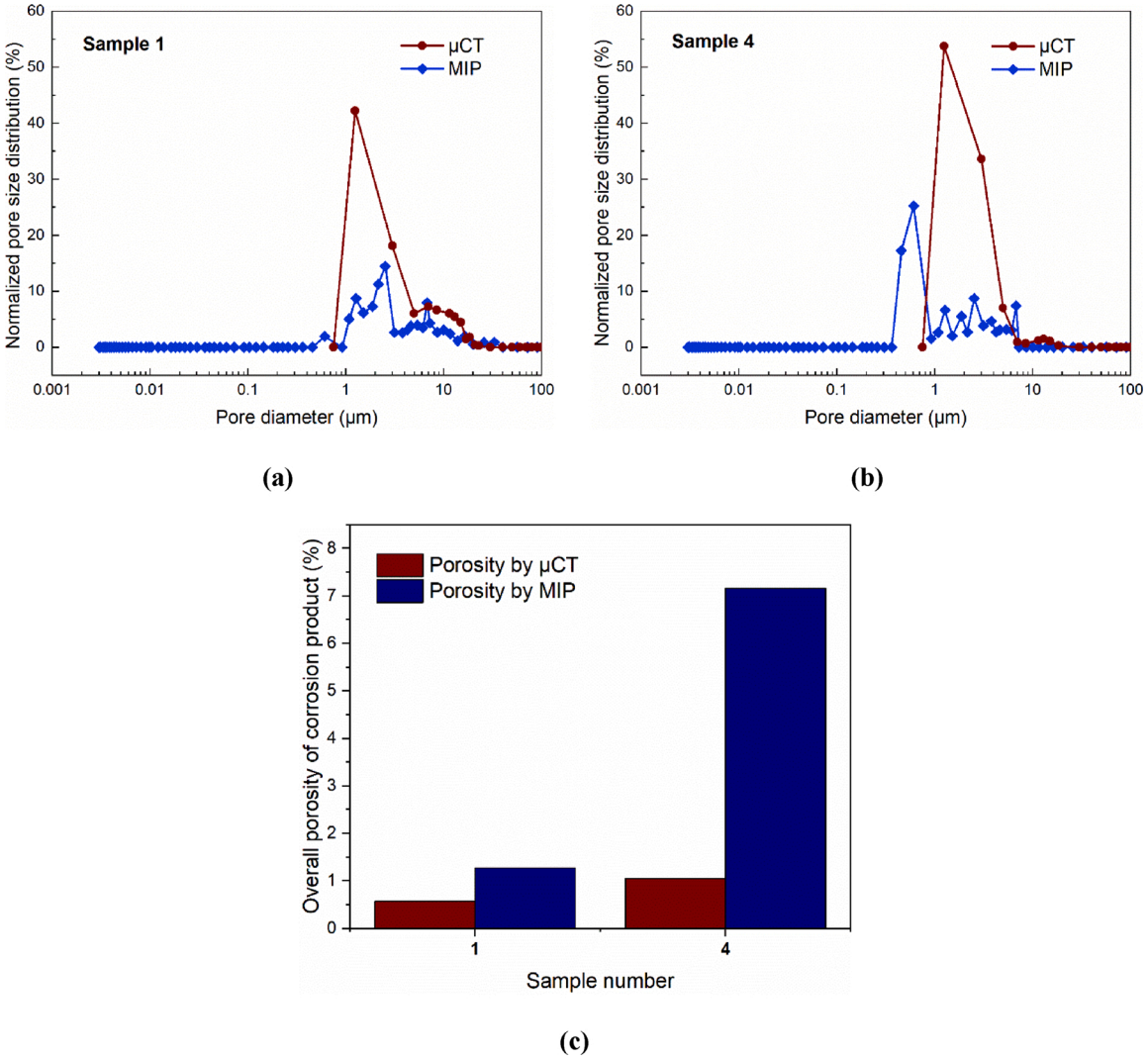

Fig. 16. Pore size distribution within the $FeCO_3$ film for **(a)** sample 1; **(b)** sample 4; **(c)** overall porosities calculated by μCT and MIP.

4.5. Pore connectivity and spatial distribution

The 3D views of the void spatial distribution for sample 1 are shown in Fig. 17. Both connected pores and isolated pores within the crystalline $FeCO_3$ layer can be observed. By using the watershed method [52], separated pores were labelled in different colours as shown in Fig. 17(c). Notably, there are some connected void clusters within the crystalline $FeCO_3$ which have a significant effect on the internal connectivity and ion transportation. By extracting a void cluster, the 3D structure of the void cluster can be observed clearly, as shown in Fig. 17(d), suggesting the void clusters provide paths for ion transportation and reduce the protectiveness of the crystalline $FeCO_3$ to the surface.

4.5.1. The relationship between connected pores and localised corrosion

To analyse the relationship between connected pores and localised corrosion sites underneath the corrosion products, the segmented steel substrate was introduced together with the connected pores, as shown in Fig. 18. Clearly, the localised corrosion was corresponding to the connected pore clusters, and localised attacks were observed along with the pores within the corrosion products for both sample 1 and sample 4. A 200 × 100 × 100 voxels sub-volume (Fig. 18(b) and (d)) was extracted from an ROI of 500 × 500 × 500 voxels to clearly observe the connected void cluster and corroded steel substrate. It can be seen that void clusters were locally extended to the steel surface, which could serve as transportation channels for corrosive species to reach the substrate. More specifically, the distribution of void clusters is non-uniform, and the shape, depth, volume and inner structure are different among void clusters. As a result, the permeability and diff ;usivity of the corrosive species could be inhomogeneous.

4.6. Comparison and limitations between μCT and MIP in pore feature characterisation

The current advantages and limitations for both μCT and MIP technique are discussed; firstly, for the μCT technique, it has detectability for the large pore sizes (the voids at micron level within this study based on spatial resolution of 0.538 μm), including both connected pores and isolated ones. In contrast, MIP is applicable to detect a wide range of connected pores, the detectable pore size range can be from several nanometres to more than 100 microns. However, in the case of highly porous structures, errors can be caused due to the breaking of the pores' walls by MIP [58], which gives distorted results. By contrast, the advantage of μCT is that it is a non-destructive method and the fragile materials remain undamaged during the μCT measurement.

Furthermore, the combined analysis of μCT and image processing provided an advantage that the pore features can be determined such as spatial connectivity in comparison to the MIP method. However, the error could be attributed to the accuracy via using image processing, as the chosen threshold for the porosity calculation was highly affected due to the outer crystalline $FeCO_3$ layer roughness. Enhancing the resolution or applying advanced image processing techniques is our future focus, enabling increased accuracy of the μCT method for pore feature characterisation.

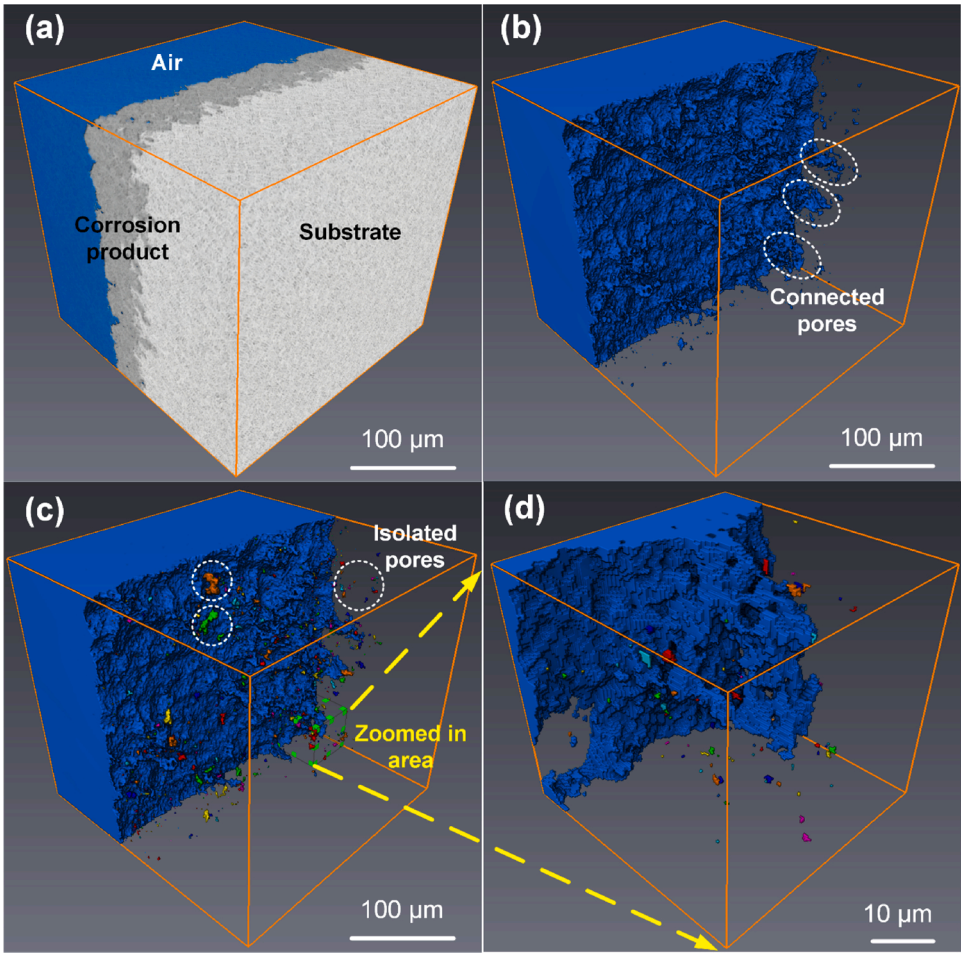

Fig. 17. Spatial distribution and connectivity of the pores for sample 1: **(a)** ROI of sample 1; **(b)** the air phase after multilevel Otsu segmentation; **(c)** pores separation in which different colours represent different isolated pores; **(d)** local enlarged pore structure within the crystalline $FeCO_3$.

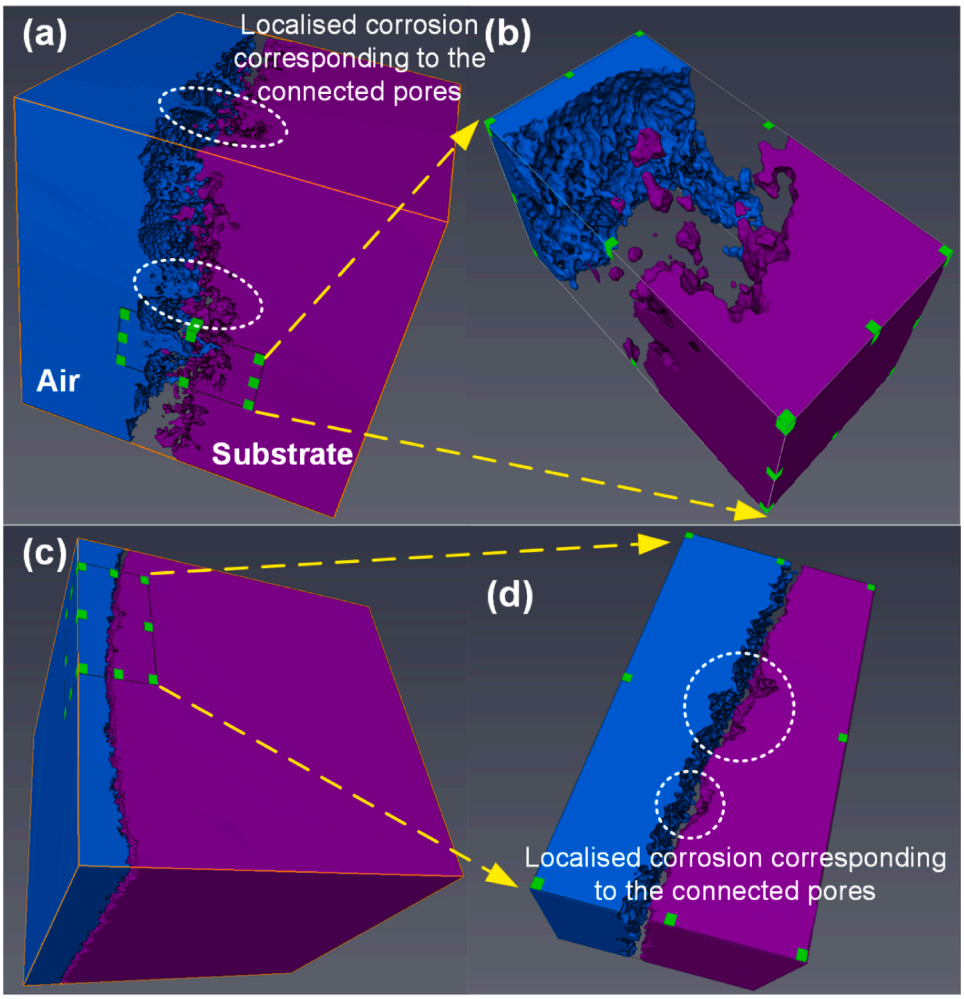

Fig. 18. The relationship between the pore distribution and localised corrosion: **(a)** connected pore distribution (blue region) and corroded steel substrate (purple region) for sample 1, with an ROI of 500 × 500 × 500 voxels (0.538 μm voxel size); **(b)** extracted sub-volume (200 × 100 × 100 voxels) from the ROI of sample 1; **(c)** connected pore distribution and corroded steel substrate for sample 4, with an ROI of 500 × 500 × 500 voxels; **(d)** extracted sub-volume (200 × 100 × 100 voxels) from the ROI of sample 4 (For interpretation of the references to colour in this figure legend, the reader is referred to the web version of this article).

5. Conclusions

μCT technique combined with image processing was applied to identify the air-voids within the $FeCO_3$ layer, and novel algorithms for thickness and porosity calculation were developed. In addition, MIP was used to validate the μCT results. Material properties of the $FeCO_3$ layer including thickness, porosity, pore size distribution and pore connectivity were determined, and the relationship with the corrosion behaviour was discussed. The following conclusions can be made:

(1) By using the new 3D method, it is found that the thickness of corrosion products follows Gaussian distribution, and the mean thickness of the $FeCO_3$ layer formed on sample 1 (90 °C and CO_2 partial pressure of 13.3 bar) is the largest at around 50.24 μm, while that for sample 3 (200 °C and CO_2 partial pressure of 2.7 bar) is the lowest at approximately 0.81 μm. Additionally, the most severe localised corrosion is found from the 3D corrosion product layer for sample 1.
(2) The overall porosities of corrosion products are 0.57 % and 1.05 % for sample 1 and sample 4 (200 °C and CO_2 partial pressure of 28.5 bar) respectively. The porosity of the outer layer is larger than that of the inner layer for both samples, indicating a more compact structure of the inner layer.
(3) Most of the voids within the $FeCO_3$ films have diameters less than 5 μm for both sample 1 and sample 4. Compared with sample 1, the voids within the crystalline $FeCO_3$ on sample 4 are mainly distributed in smaller pore diameters of sub-micron level.
(4) Direct evidence was observed for the relevance between localised corrosion and connected pores from the μCT results. The connected void clusters deep into the steel surface providing transportation channels for corrosive species, possibly inducing localised attack.
(5) The overall porosity and pore size distribution calculation by μCT were compared with MIP method, indicating the feasibility of μCT in corrosion product characterisation yet suggesting greater resolution is required to fully resolve and characterise pore size distribution and connectivity.

CRediT authorship contribution statement

Cailin Wang: Conceptualization, Data curation, Formal analysis, Investigation, Methodology, Writing - original draft. **Yong Hua:** Conceptualization, Data curation, Formal analysis, Investigation, Methodology, Writing - original draft. **Sadegh Nadimi:** Conceptualization, Data curation, Formal analysis, Investigation, Methodology, Writing - original draft. **Wassim Taleb:** Investigation, Visualization, Writing - review & editing. **Richard Barker:** . **Yuxing Li:** Investigation, Visualization, Writing - review & editing. **Xiaohui Chen:** Investigation, Visualization, Writing - review & editing. **Anne Neville:** Writing - review & editing, Funding acquisition, Supervision.

Declaration of Competing Interest

The authors declare that they have no known competing financial interests or personal relationships that could have appeared to influence

the work reported in this paper.

Acknowledgement

This research is part of a project that has received funding from the European Research Council (ERC) under the European Union's Horizon 2020 research and innovation programme (Grant agreement No. 742930).

References

[1] S. Nesic, Key issues related to modelling of internal corrosion of oil and gas pipelines - a review, Corros. Sci. 49 (12) (2007) 4308–4338.
[2] Y. Hua, R. Barker, A. Neville, Comparison of corrosion behaviour for X65 carbon steel in supercritical CO_2-saturated water and water-saturated/unsaturated supercritical CO_2, J. Supercrit. Fluids 97 (2015) 224–237.
[3] C. Wang, Y. Li, L. Teng, S. Gu, Q. Hu, D. Zhang, X. Ye, J. Wang, Experimental study on dispersion behavior during the leakage of high pressure CO_2 pipelines, Exp. Therm. Fluid Sci. 105 (2019) 77–84.
[4] L. Teng, Y. Li, Q. Hu, D. Zhang, X. Ye, S. Gu, C. Wang, Experimental study of near-field structure and thermo-hydraulics of supercritical CO_2 releases, Energy 157 (2018) 806–814.
[5] Y. Hua, R. Barker, A. Neville, The influence of SO_2 on the tolerable water content to avoid pipeline corrosion during the transportation of supercritical CO_2, Int. J. Greenh. Gas Control 37 (2015) 412–423.
[6] Y. Hua, R. Barker, A. Neville, The effect of O_2 content on the corrosion behaviour of X65 and 5Cr in water-containing supercritical CO_2 environments, Appl. Surf. Sci. 356 (2015) 499–511.
[7] S. Gu, Y. Li, L. Teng, Q. Hu, D. Zhang, X. Ye, C. Wang, J. Wang, S. Iglauer, A new model for predicting the decompression behavior of CO_2 mixtures in various phases, Process Saf. Environ. 120 (2018) 237–247.
[8] A. Shamsa, R. Barker, Y. Hua, E. Barmatov, T. Hughes, A. Neville, The role of Ca^{2+} ions on Ca/Fe carbonate products on X65 carbon steel in CO_2 corrosion environments at 80 and 150 °C, Corros. Sci. 156 (2019) 58–70.
[9] L. Wei, X. Pang, C. Liu, K. Gao, Formation mechanism and protective property of corrosion product scale on X70 steel under supercritical CO_2 environment, Corros. Sci. 100 (2015) 404–420.
[10] Y.C. Zhang, X.L. Pang, S.P. Qu, X. Li, K.W. Gao, Discussion of the CO_2 corrosion mechanism between low partial pressure and supercritical condition, Corros. Sci. 59 (2012) 186–197.
[11] Y. Hua, R. Barker, A. Neville, Effect of temperature on the critical water content for general and localised corrosion of X65 carbon steel in the transport of supercritical CO_2, Int. J. Greenh. Gas Control 31 (2014) 48–60.
[12] M.H. Sk, A.M. Abdullah, M. Ko, B. Ingham, N. Laycock, R. Arul, D.E. Williams, Local supersaturation and the growth of protective scales during CO_2 corrosion of steel: effect of pH and solution flow, Corros. Sci. 126 (2017) 26–36.
[13] Y. Hua, R. Barker, T. Charpentier, M. Ward, A. Neville, Relating Iron carbonate morphology to corrosion characteristics for water-saturated supercritical CO_2 systems, J. Supercrit. Fluids 98 (2014) 183–193.
[14] C. Palacios, J. Shadley, Characteristics of corrosion scales on steels in a CO_2-saturated NaCl brine, Corrosion 47 (2) (1991) 122–127.
[15] J. Sun, W. Liu, W. Chang, Z.H. Zhang, Z.T. Li, T. Yu, M.X. Lu, Characteristics and formation mechanism of corrosion scales on low-chromium X65 steels in CO_2 environment, Acta Metall. Sin. 45 (1) (2009) 84–90.
[16] D.W. Shannon, Role of chemical components in geothermal brine on corrosion, NACE Corrosion (1978).
[17] J. Han, D. Young, H. Colijn, A. Tripathi, S. Nesic, Chemistry and structure of the passive film on mild steel in CO_2 corrosion environments, Ind. Eng. Chem. Res. 48 (13) (2009) 6296–6302.
[18] A. Dugstad, Fundamental aspects of CO2 metal loss corrosion - part 1: mechanism, Corrosion (2006) (San Diego, CA: NACE International Conference) (2006).
[19] Z. Yin, Y. Feng, W. Zhao, Z. Bai, G. Lin, Effect of temperature on CO_2 corrosion of carbon steel, Surf. Interface Anal. 41 (6) (2009) 517–523.
[20] Y. Hua, S. Xu, Y. Wang, W. Taleb, J. Sun, L. Zhang, R. Barker, A. Neville, The formation of $FeCO_3$ and Fe_3O_4 on carbon steel and their protective capabilities against CO_2 corrosion at elevated temperature and pressure, Corros. Sci. 157 (2019) 392–405.
[21] K. Videm, A. Dugstad, Film covered corrosion, film breakdown and pitting attack of carbon steels in aqueous CO_2 environments, Corrosion (1988). Houston, TX: NACE, 1988.
[22] W. Sun, K. Chokshi, S. Nesic, D.A. Gulino, A Study of Protective Iron Carbonate Scale Formation in CO_2 Corrosion, AIChE, Austin, Texas, 2004.
[23] D. Li, Y. Feng, Z. Bai, M. Zheng, Characteristics of CO_2 corrosion scale formed on N80 steel in stratum water with saturated CO_2, Appl. Surf. Sci. 253 (20) (2007) 8371–8376.
[24] M. Gao, X. Pang, K. Gao, The growth mechanism of CO_2 corrosion product films, Corros. Sci. 53 (2) (2011) 557–568.
[25] S. Nesic, K.L.J. Lee, A mechanistic model for carbon dioxide corrosion of mild steel in the presence of protective iron carbonate films—part 3: film growth model, Corrosion 59 (7) (2003) 616–628.
[26] A. Kahyarian, M. Singer, S. Nesic, Modeling of uniform CO_2 corrosion of mild steel in gas transportation systems: a review, J. Nat. Gas Sci. Eng. 29 (2016) 530–549.
[27] W. Sun, S. Nesic, Kinetics of corrosion layer formation: part 1-iron carbonate layers in carbon dioxide corrosion, Corrosion 64 (4) (2008) 334–346.
[28] A.B. Abell, K.L. Willis, D.A. Lange, Mercury intrusion porosimetry and image analysis of cement-based materials, J. Colloid Interf. Sci. 211 (1999) 39–44.
[29] Y. Yao, D. Liu, Comparison of low-field NMR and mercury intrusion porosimetry in characterizing pore size distributions of coals, Fuel 95 (2012) 152–158.
[30] H. Ma, Mercury intrusion porosimetry in concrete technology: tips in measurement, pore structure parameter acquisition and application, J. Porous Mat. 21 (2) (2014) 207–215.
[31] G. Zgrablich, S. Mendioroz, L. Daza, J. Pajares, V. Mayagoitia, F. Rojas, W. C. Conner, Effect of porous structure on the determination of pore size distribution by mercury porosimetry and nitrogen sorption, Langmuir 7 (4) (1991) 779–785.
[32] S.P. Rigby, R.S. Fletcher, S.N. Riley, Characterisation of porous solids using integrated nitrogen sorption and mercury porosimetry, Chem. Eng. Sci. 59 (1) (2004) 41–51.
[33] N.D. Ferro, P. Delmas, C. Duwig, G. Simonetti, F. Morari, Coupling X-ray microtomography and mercury intrusion porosimetry to quantify aggregate structures of a cambisol under different fertilisation treatments, Soil Till. Res. 119 (2012) 13–21.
[34] S. Chung, T. Han, S. Kim, T. Lee, Investigation of the permeability of porous concrete reconstructed using probabilistic description methods, Constr. Build. Mater. 66 (2014) 760–770.
[35] N. Bossa, P. Chaurand, J. Vicente, D. Borschneck, C. Levard, O.A. Aguerre-Chariol, J. Rose, Micro- and nano-X-ray computed-tomography: a step forward in the characterization of the pore network of a leached cement paste, Cement Concrete Res. 67 (2015) 138–147.
[36] Y. Wang, J. Dai, X-ray computed tomography for pore-related characterization and simulation of cement mortar matrix, NDT & E Int. 86 (2017) 28–35.
[37] S. Nadimi, J. Fonseca, Image based simulation of one-dimensional compression tests on carbonate sand, Meccanica 54 (4–5) (2019) 697–706.
[38] S. Nadimi, A. Ghanbarzadeh, A. Hassanpour, A. Neville, A discussion on the capability of X-ray computed tomography for contact mechanics investigations (F. Zhang, J. Liu, X. Ding, Z. Yang, Tribol. Int. 145 (2020) 106167), Tribol. Int. (2020), 106433.
[39] P. Itty, M. Serdar, C. Meral, D. Parkinson, A. MacDowell, D. Bjegovic, P. Monteiro, In situ 3D monitoring of corrosion on carbon steel and ferritic stainless steel embedded in cement paste, Corros. Sci. 83 (2014) 409–418.
[40] S. Ghahari, A. Davenport, T. Rayment, T. Suter, J. Tinnes, C. Padovani, J. Hammons, M. Stampanoni, F. Marone, R. Mokso, In situ synchrotron X-ray micro-tomography study of pitting corrosion in stainless steel, Corros. Sci. 53 (9) (2011) 2684–2687.
[41] F. Almuaili, S. McDonald, P. Withers, D. Engelberg, Application of a quasi in situ experimental approach to estimate 3-D pitting corrosion kinetics in stainless steel, J. Electrochem. Soc. 163 (13) (2016) C745–C751.
[42] F. Farhad, D. Smyth-Boyle, X. Zhang, I. Wallis, D. Panggabean, Laboratory apparatus for in-situ corrosion fatigue testing and characterisation of fatigue cracks using X-ray micro-computed tomography, Fatigue Fract. Eng. M 41 (12) (2018) 2629–2637.
[43] R. Rizzo, S. Baier, M. Rogowska, R. Ambat, An electrochemical and X-ray computed tomography investigation of the effect of temperature on CO_2 corrosion of 1Cr carbon steel, Corros. Sci. 166 (2020), 108471.
[44] S.R. Stock, N.K. Naik, A.P. Wilkinson, K.E. Kurtis, X-ray microtomography (microCT) of the progression of sulfate attack of cement paste, Cement Concrete Res. 32 (10) (2002) 1673–1675.
[45] J. Fonseca, S. Nadimi, C.C. Reyes-Aldasoro, M.R. Coop, Image-based investigation into the primary fabric of stress-transmitting particles in sand, Soils Found. 56 (5) (2016) 818–834.
[46] S. Nadimi, J. Fonseca, E. Andò, G. Viggiani, A micro finite-element model for soil behaviour: experimental evaluation for sand under triaxial compression, Géotechnique (2019) 1–6.
[47] K. Kapat, P.K. Srivas, A.P. Rameshbabu, P.P. Maity, S. Jana, J. Dutta, P. Majumdar, D. Chakrabarti, S. Dhara, Influence of porosity and pore-size distribution in Ti_6Al_4V foam on physicomechanical properties, osteogenesis, and quantitative validation of bone ingrowth by micro-computed tomography, ACS Appl. Mater. Inter. 9 (45) (2017) 39235–39248.
[48] J.B. LeBret, M.G. Norton, D.F. Bahr, Examination of crystal defects with high-kV X-ray computed tomography, Mater. Lett. 59 (2005) 1113–1116.
[49] X. Zhang, S. Aliasghari, A. Němcová, T.L. Burnett, I. Kuběna, M. Smid, G. E. Thompson, P. Skeldon, P.J. Withers, X-ray computed tomographic investigation of the porosity and morphology of plasma electrolytic oxidation coatings, ACS Appl. Mater. Inter. 8 (13) (2016) 8801–8810.
[50] N. Otsu, A threshold selection method from gray-level histograms, IEEE T. Syst. Man Cy. 9 (1) (1979) 62–66.
[51] A.K.M. Khairuzzaman, S. Chaudhury, Multilevel thresholding using grey wolf optimizer for image segmentation, Expert Syst. Appl. 86 (2017) 64–76.
[52] L. Vincent, P. Soille, Watersheds in digital spaces: an efficient algorithm based on immersion simulations, IEEE T. Pattern Anal. 6 (1991) 583–598.
[53] J. Canny, A computational approach to edge detection, IEEE T. Pattern Anal. 6 (1986) 679–698.
[54] A.C.G.-1 on C. of Metals, Standard practice for preparing, cleaning, and evaluating corrosion test specimens, ASTM Int. (2011).
[55] S. Nesic, J.M. Nordsveen, R. Nyborg, A. Stangeland, A mechanistic model for CO_2 corrosion with protective iron carbonate films, CORROSION/2001, Paper No. 40, NACE, Houston, TX (2001).

[56] W. Sun, S. Nesic, R.C. Woollam, The effect of temperature and ionic strength on iron carbonate ($FeCO_3$) solubility limit, Corros. Sci. 51 (6) (2009) 1273–1276.
[57] J. Zhou, G. Ye, K.V. Breugel, Characterization of pore structure in cement-based materials using pressurization-depressurization cycling mercury intrusion porosimetry (PDC-MIP), Cement Concrete Res. 40 (7) (2010) 1120–1128.
[58] L. Korat, V. Ducman, A. Legat, B. Mirtic, Characterisation of the pore-forming process in lightweight aggregate based on silica sludge by means of X-ray micro-tomography (micro-CT) and mercury intrusion porosimetry (MIP), Ceram. Int. 39 (6) (2013) 6997–7005.